PCCP

RSC Publishing

PAPER

View Article Online
View Journal | View Issue

Cite this: *Phys. Chem. Chem. Phys.*, 2013, **15**, 7260

First principles calculations of the structure and V L-edge X-ray absorption spectra of V_2O_5 using local pair natural orbital coupled cluster theory and spin–orbit coupled configuration interaction approaches

Dimitrios Maganas,[a] Michael Roemelt,[a] Michael Hävecker,[bc] Annette Trunschke,[b] Axel Knop-Gericke,[b] Robert Schlögl[ab] and Frank Neese*[a]

A detailed study of the electronic and geometric structure of V_2O_5 and its X-ray spectroscopic properties is presented. Cluster models of increasing size were constructed in order to represent the surface and the bulk environment of V_2O_5. The models were terminated with hydrogen atoms at the edges or embedded in a Madelung field. The structure and interlayer binding energies were studied with dispersion-corrected local, hybrid and double hybrid density functional theory as well as the local pair natural orbital coupled cluster method (LPNO-CCSD). Convergence of the results with respect to cluster size was achieved by extending the model to up to 20 vanadium centers. The O K-edge and the V $L_{2,3}$-edge NEXAFS spectra of V_2O_5 were calculated on the basis of the newly developed Restricted Open shell Configuration Interaction with Singles (DFT-ROCIS) method. In this study the applicability of the method is extended to the field of solid-state catalysis. For the first time excellent agreement between theoretically predicted and experimentally measured vanadium L-edge NEXAFS spectra of V_2O_5 was achieved. At the same time the agreement between experimental and theoretical oxygen K-edge spectra is also excellent. Importantly, the intensity distribution between the oxygen K-edge and vanadium L-edge spectra is correctly reproduced, thus indicating that the covalency of the metal–ligand bonds is correctly described by the calculations. The origin of the spectral features is discussed in terms of the electronic structure using both quasi-atomic jj coupling and molecular LS coupling schemes. The effects of the bulk environment driven by weak interlayer interactions were also studied, demonstrating that large clusters are important in order to correctly calculate core level absorption spectra in solids.

Received 15th February 2013,
Accepted 11th March 2013

DOI: 10.1039/c3cp50709b

www.rsc.org/pccp

Introduction

Near edge X-ray absorption fine structure (NEXAFS) spectroscopy is a powerful technique to study the electronic and geometric structures of materials in an element specific fashion.[1] Moreover, core electron spectroscopy is not limited to studies of crystalline materials but it can also be applied to amorphous matter, in order to detect trace amounts of elements in the sub-nanometer scale. In terms of a simple one-electron picture, the spectral features arise from the excitation of a core electron to the lowest unoccupied orbitals (LUMOs) of the material under investigation. The relevant absorption processes are governed by the usual dipole selection rules. Thus, the K-edge spectral region is dominated by $1s \rightarrow 2p$ dipole transitions, whereas the $L_{2,3}$ spectral region mainly corresponds to transitions between the fully occupied 2p-core orbitals and partially filled or empty 3d-based orbitals. Being based on electric dipole allowed transitions, transition metal L-edge spectra are typically richly structured. They are, however, also difficult to interpret since on top of ligand-field and covalency effects, one must consider spin–orbit coupling (SOC) between the potentially many final state multiplets. The latter dominates the spectra and splits them into the so-called L_3 and L_2 edges. Therefore, with rare exceptions, L-edge spectra cannot be successfully interpreted on the basis of a simple one-electron picture, despite the fact that they contain a wealth of information on geometric and electronic structure.[1,2] In order to extract such information, an efficient theoretical methodology with predictive accuracy and

[a] *Max-Planck Institute for Chemical Energy Conversion, Stiftsrasse 34-36, Mülheim an der Ruhr, D-45470, Germany. E-mail: frank.neese@cec.mpg.de*
[b] *Inorganic Chemistry Department, Fritz-Haber-Institut der Max-Planck-Gesellschaft, Faradayweg 4-6, 14195 Berlin, Germany*
[c] *Helmholtz-Zentrum Berlin/BESSY II, Division Solar Energy Research, Albert-Einstein-Str. 15, 12489 Berlin, Germany*

without adjustable parameters is required. First principles calculations within the framework of various particle/hole approximations, including multiple scattering[3] and TD-DFT[4–6] approaches, have been proven successful in interpreting K-edge spectra but have met with at best limited success in the case of $L_{2,3}$-edge spectra. In particular, for transition metal $L_{2,3}$-edge spectra the particle/hole based theories have very limited predictive capabilities. This is already evident for the case at hand, V_2O_5, for which, despite several attempts,[7–9] to date no successful calculation of the vanadium L-edge absorption spectrum has been reported. Given that this material formally contains $V^{(V)}$ sites with a d^0 closed-shell electronic configuration, this is somewhat surprising. We will come back to this point in the discussion.

Several theoretical methods for the calculation of transition metal L-edge spectra have been reported in the literature. Clearly, the shape of the $L_{2,3}$ spectra is strongly affected by the coordination environment of the metal and therefore the necessity emerges for more efficient methodologies, which involve relativistic effects and describe the metal–ligand covalent bonding in detail. Methods that attempt a more detailed modelling involve the semiempirical ligand field multiplet (LFM) and charge transfer multiplet (CTM) methods. CTM and LFM methods incorporate crystal field effects into an atomic multiplet calculation, using a group theoretical formalism.[1,10–12] A large number of successful applications have been reported on the basis of these methods. The drawback of such methodologies is the large number of semi-empirical parameters that are necessary to describe the ligand field, inter-electronic repulsion and covalency at the metal site. Without a clearcut way to predict these parameters from first-principles calculations, those methods are best used as tools for data analysis and to obtain insight into spectral trends through systematic variation of the semi-empirical parameters.[1,10,13] The CTM method is computationally highly efficient but cannot handle cluster models including multiple transition metals and is thus limited in its ability to reproduce real solid state phenomena. An *ab initio* method that does not rely on empirical parameters is the *ab initio* CTM method developed by Tanaka *et al*.[14] In this method configuration interaction (CI) is performed using two-component molecular spinors calculated with relativistic density functional theory (DFT). While being rigorous if performed to completion, it is difficult in this approach to ensure that for truncated CI spaces the space of excited determinants indeed spans the correct space of the final state multiplets. The computational cost of the method is reported to be very high, such that only systems with a few atoms in the unit cell can presently be treated.[14–17] Alternative techniques that account for electron correlation between 3d and 2p core-electrons have been reported recently, but they do not properly treat the final state multiplet structure.[18–20] In addition, Haverkort and co-workers have performed CI calculations based on plane-wave DFT, using projection methods to obtain a localized expansion space,[21] while Bagus has performed CI calculations on top of an atomic-four component relativistic self-consistent field calculations.[22] Both of these approaches appear to be restricted to highly symmetric molecules and require significant computational resources.

Our approach to the problem of calculating transition metal L-edge spectra with predictive accuracy relies on a wavefunction methodology that has been developed in the framework of molecular quantum chemistry. The recently developed DFT/Restricted Open shell Configuration Interaction Singles method (DFT/ROCIS)[23] can be applied to systems with 100–200 atoms and, hence, substantial cluster models are within reach on the standard present day hardware. The method treats all multiplet effects correctly and incorporates spin–orbit coupling in a fairly rigorous form using QDPT in combination with a mean-field approximation to the full two-body SOC operator.[24–26] Since Hartree–Fock orbitals are of very poor quality for transition metal complexes, the method uses DFT orbitals. Furthermore, it is only slightly parameterized in order to implicitly account for the remaining missing dynamic electron correlation effects. Three universal parameters have been introduced for the entire periodic table and have been fixed through extensive test calculations on a series of first row transition metal complexes. Encouraged by the excellent performance of DFT/ROCIS for a series of mononuclear transition metal complexes,[23] the method is applied here for the first time to a challenging solid-state system.

The system of choice is vanadium pentoxide, V_2O_5. This compound is a member of a large vanadium oxide family, *e.g.* VO, VO_2, V_2O_3, in which the oxidation state of vanadium ranges between +2 and +5. The broad range of accessible oxidation states is accompanied by a large variety of geometric and electronic structures and, hence, also by a wide range of molecular properties as well as reactivities. Together with the high abundance of vanadium this renders vanadium oxides interesting for scientific studies as well as industrial applications. In fact V_2O_5 is involved in the reduction of NO_x by NH_3[27] or in the selective oxidation of hydrocarbons.[28,29] In addition, it is an active participant in thermally/electrically activated optical switching devices, write–erase media, optical waveguides and microreactor catalyst beds.[27,30] Moreover, the readily accessible $V^{(V)}/V^{(IV)}$ redox couple makes it an especially attractive system for use as a cathode material in Li-ion batteries.[31–33] For most of these applications, NEXAFS spectroscopy has been proven a very useful technique to monitor the catalytic activity and probe the electronic structure of this very important catalyst. As a result, a large library of V L-edge and K O-edge NEXAFS spectra under several experimental conditions exists. Several theoretical studies have been successful in reproducing the K O-edge spectral region.[34–36] However, so far no relevant study has been successful in properly reproducing the V L-edge part of the spectrum.[7–9] Herein, we apply the DFT/ROCIS method in conjunction with a large cluster model and demonstrate that excellent agreement with experiment can be obtained without the variation of any adjustable parameter.

Core electron spectroscopy of V_2O_5

In a simple one-electron picture the dipole selection rules for NEXAFS require that there is no change in the spin of the excited electron and that the change in the angular momentum quantum number is $\Delta l = \pm 1$.[37,38] This implies that for the

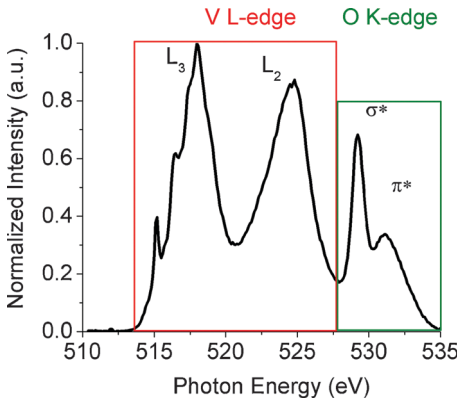

Fig. 1 V L-edge and O K-edge total electron yield NEXAFS spectrum of V_2O_5.[39]

excitation of an O-1s electron, only transitions into acceptor orbitals with some O-2p character have non-zero intensity. Thus, the oxygen K-edge (O-1s → O-2p) and metal L-edge (M = V, V-2p → V-3d) regions of NEXAFS provide a sensitive and complementary probe of the electronic structure of the transition metal oxides. In the case of vanadium oxides, the relative positions of the V L- and O K-edges are such that these spectra partially overlap. The combined experimental V L-edge and O K-edge spectrum of V_2O_5 is presented in Fig. 1.[39] Given the dipole transition selection rules described above, the V L-edge NEXAFS spectra represent transitions into the empty or half-occupied V-3d based orbitals, whereas the O K-edge spectra provide information about the oxygen p-character in the low-lying half-occupied or unoccupied orbitals. The two broad peaks centered at ~518 and 525 eV are the V-L_3 and V-L_2 peaks. In a jj coupling picture, they are assigned to V-$2p_{3/2}$ → V-3d and V-$2p_{1/2}$ → V-3d transitions, respectively. The spin–orbit splitting between the V-L_3 and V-L_2 peaks is ~7 eV for the V_2O_5 single crystal, similar to the 6.9 eV spitting observed in the V L-edge NEXAFS spectrum of V_2O_5 nanowires[40] and to the 7.5 eV splitting observed in V-2p X-ray photoelectron spectroscopy (XPS).[40] The differences in the observed spin–orbit splittings have been attributed to the different final states reached by the various processes. In addition, the V-L_2 peak is broadened by a Coster–Kronig Auger decay process[41] into the $2p_{3/2}$ hole and is less informative than the corresponding V-L_3 peak in interpreting the electronic structure of V_2O_5. In fact the V-L_3 peaks show considerable fine structure that depends on the angle enclosed by the molecular axes and the polarization vector E of the incident beam. The fine structured peaks observed are due to the specific orientation of the half-occupied and unoccupied metal d-based orbitals as dictated by the ligand field. In addition, as the O-2p orbitals are highly mixed with those of the corresponding V-3d orbitals, due to covalent bonding these transitions are finely structured (529, 531 eV). The most intense peak (529 eV) corresponds to transitions from the O-1s to O-$2p_{xy}$ + V t_{2g}-like orbitals (d_{xy}, d_{yz}, d_{xz}), whereas the higher energy component (531 eV), corresponds to transitions from the O-1s to O-$2p_z$ + V e_g-like orbitals (d_{z2}, d_{x2-y2}). As a result, this part of the spectrum is also highly sensitive to polarization and it has been thoroughly investigated by various experimental and theoretical methods.[34,40,42,43] In this study both powder and single crystal spectra of V_2O_5 are analyzed in detail. The experimental treatment of the powder samples as well as crystal growing and X-ray absorption measurement conditions have been described previously.[44,45]

Theory

DFT/ROCIS is based on an *ab initio* version of a molecular LS coupling scheme. Within the DFT/ROCIS Ansatz, one tries to combine the best of the DFT and wavefunction-based quantum chemistry worlds: (i) A good description of the orbitals and metal ligand covalency derived by DFT calculations and (ii) the correct spin-coupling, multiplet structure and spin–orbit coupling treatment of multideterminantal wavefunction-based methods. The theoretical and computational aspects of this method have been thoroughly discussed recently.[23] In a nutshell, the solution of the open-shell spin restricted Kohn–Sham (ROKS) equations is performed in order to obtain a restricted set of molecular orbitals. The orbital set is divided into a set of doubly occupied orbitals (DOMOs) and a set of singly occupied orbitals (SOMOs), which are eigenvectors of the two Kohn–Sham matrices

$$\begin{aligned} F_{pq}^{C(KS)} &= h_{pq} - c_{DF} V_{pq}^{XC}[\rho] + \sum_{i}^{DOMOs} 2J_{pq}^{ii} - c_{HF} K_{pq}^{ii} \\ &\quad + \sum_{t}^{SOMOs} J_{pq}^{tt} - \frac{c_{HF}}{2} K_{pq}^{tt} \\ F_{pq}^{O(KS)} &= h_{pq} - c_{DF} V_{pq}^{XC}[\rho] + \sum_{i}^{DOMOs} 2J_{pq}^{ii} - c_{HF} K_{pq}^{ii} \\ &\quad + \sum_{t}^{SOMOs} J_{pq}^{tt} - c_{HF} K_{pq}^{tt} \end{aligned} \tag{1}$$

Here, $h_{pq} = \langle \phi_p | \hat{h} | \phi_q \rangle$ are integrals of molecular orbitals ϕ_p and ϕ_q over the one-electron part of the BO-Hamiltonian. As usual, labels i, j, k refer to doubly occupied orbitals of the reference determinant, a, b, c, d refer to empty orbitals, t, u, v, w denote singly occupied orbitals and labels p, q, r, s are used for any set of orbitals. The two-electron integrals are stored in matrices of the form

$$\begin{aligned} J_{pq}^{ii} &= (ii|pq) = \int \phi_i^*(1)\phi_i(1)\frac{1}{r_{12}}\phi_p^*(2)\phi_q(2)d\tau_1 d\tau_2 \\ K_{pq}^{ii} &= (ip|iq) = \int \phi_i^*(1)\phi_p(1)\frac{1}{r_{12}}\phi_i^*(2)\phi_q(2)d\tau_1 d\tau_2 \end{aligned} \tag{2}$$

Moreover, $V_{pq}^{XC}[\rho] = \left\langle \phi_p \middle| \frac{\delta E_{XC}[\rho]}{\delta \rho} \middle| \phi_q \right\rangle$ denotes elements of the exchange–correlation matrix that depends on the actual density functional used. Both matrices are given in the hybrid density functional form, since hybrid density functionals will be used in all presented DFT/ROCIS calculations. The coefficients c_{HF} and c_{DF} denote the amount of HF exchange and pure density functional related exchange–correlation contribution, respectively. Accordingly, for a HF calculation $c_{DF} = 0$. The DFT/ROCIS method implicitly introduces dynamic electron correlation

through a set of three semi-empirical parameters c_1, c_2, and c_3. They scale the Coulomb and Exchange integrals in the diagonal of the CI matrix, as well as the off-diagonal elements, respectively. For example, in the subspace spanned by the $|\Psi_i^{\alpha}\rangle$ basis functions the CI matrix elements become:

$$H_{ia,ia}^{DFT/ROCIS} = F_{aa}^{C(KS)} - F_{ii}^{C(KS)} - c_1(ii|aa) + 2c_2(ii|bb) \quad (3)$$

$$H_{ia,ib}^{DFT/ROCIS} = c_3\{\delta_{ij}F_{ab}^{C(KS)} - \delta_{ab}F_{ij}^{C(KS)}(ii|ab) - 2(ia|ja)\} \quad (4)$$

As discussed above, the parameters c_1, c_2, and c_3 were optimized with respect to a test set of first row transition metal L-edges including titanium, vanadium and iron in a variety of oxidation and spin states. Minimization of the root-mean-square deviation between calculated and experimental transition metal L_3-edge spectra yielded c_1 = 0.18, c_2 = 0.20 and c_3 = 0.40 as the best set of parameters. A detailed analysis regarding the chosen test set and the minimization procedure is described elsewhere.[23] It should be noted that such an empirical scaling is in the general spirit of the DFT method and it is well distinguished from the definition of the empirical parameters in semiempirical MO theories.

These orbitals are then fed into the ROCIS equations for the calculation of the molecular LS multiplets through configuration interaction (CI) with space- and spin-symmetry adapted configuration state functions (CSFs). Due to strong 2p SOC in the final state manifold it is necessary to calculate excited states that feature different spin quantum numbers than the ground state total spin S. The Ansatz for the three different classes of ROCIS wavefunctions is

$$\left|\Psi^{S'=S}\right\rangle = \sum_{it} c_i^t\left|\Phi_i^t\right\rangle + \sum_{ia} c_i^a\left|\Phi_i^a\right\rangle \sum_{ita} c_{ti}^{at}\left|\Phi_{ti}^{at}\right\rangle \sum_{itwa} c_{wi}^{at}\left|\Phi_{wi}^{at}\right\rangle \quad (5)$$

$$\left|\Psi^{S'=S-1}\right\rangle = \sum_{it} c_i^t\left|\Phi_i^{t(-)}\right\rangle + \sum_{ia} c_i^a\left|\Phi_i^{a(-)}\right\rangle \quad (6)$$

$$\left|\Psi^{S'=S+1}\right\rangle = \sum_{ia} c_i^a\left|\Phi_i^{a(+)}\right\rangle \quad (7)$$

Here i,j,k,l... indices denote donor orbitals, t,u,v,w indices correspond to singly occupied orbitals, whereas indices a,b,c,d... refer to orbitals that are unoccupied in the reference determinant. The excited CSF's $\{|\Phi\rangle\}$ are generated with the aid of second quantized replacement and spin operators, as explained elsewhere.[23] The three blocks of the CI matrix are diagonalized separately for a prespecified number of roots.

In the following QDPT treatment, one starts with the non-relativistic ROCIS states in the form of $\left|\Psi_{ROCIS}^{SS}\right\rangle = \sum_{\mu} C_{\mu I}\left|\Phi_{\mu}^{SS}\right\rangle$. The upper indices SS denote a many-particle wavefunction with spin quantum number S and spin projection quantum number M=S. Since the BO Hamiltonian does not contain any complex valued operator, the $|\Psi_I^{SS}\rangle$ solutions may be chosen to be real-valued. This basis is then extended to the set of functions $|\Psi_I^{SM}\rangle$ in which I covers all the roots calculated in the first step of the procedure and M = −S···S enumerates all members of a given spin multiplet. Matrix elements over the $|\Psi_I^{SM}\rangle$ functions are readily generated using the Wigner–Eckart theorem.[46]

On the basis of the above functions, SOC can be included by means of quasi-degenerate perturbation theory (QDPT), which amounts to the diagonalization of the matrix representation of $\hat{H}_{BO} + \hat{H}_{SOC}$, in the basis of the states $|\Psi_I^{SM}\rangle$:

$$\left\langle \Psi_I^{SM}\middle|\hat{H}_{BO} + \hat{H}_{SOC}\middle|\Psi_J^{S'M'}\right\rangle = \delta_{IJ}\delta_{SS'}\delta_{MM'}E_I^{(S)} + \left\langle \Psi_I^{SM}\middle|\hat{H}_{SOC}\middle|\Psi_J^{S'M'}\right\rangle \quad (8)$$

Diagonalization of this matrix yields the relativistic energy levels and eigenvectors that are used to compute the actual L-edge spectra. The spin–orbit operator used is the molecular spin–orbit mean field (SOMF) operator in the implementation already described[26] which has been shown to provide good results for spin–orbit effects for valence shell properties.[47,48] To the best of our knowledge, QDPT has never been used to calculate transition metal core-level SOC effects.

It should be noted that the absolute transition energies carry large but highly systematic errors that arise from shortcomings of the density functionals in the core region, limitations of the basis set and shortcomings in the accurate modeling of spin-free (scalar) relativistic effects. Since the deviations are highly systematic, all these factors can (for a given basis set and density functional) be taken into account by introducing an element-dependent shift.[4,13,49] Several calibration studies have already been reported for metal- and ligand K-edges.[4,5,50–52] This calibration needs to be carried out with respect to a training set of well-known systems. In the case of vanadium, this calibration will be reported in a separate study.[53] In this work we take the liberty to treat the shift as an empirical parameter.

Computational details

All calculations were performed by the ORCA suit of programs.[54] The BP86[55,56] and B3LYP[55,57,58] functionals were used together with the Grimme's dispersion correction[59,60] for geometries/frequencies and electronic properties, respectively. The Ahlrichs polarized def2-TZVP[61,62] basis sets of triple ζ quality[63] for all the atoms in combination with the def2-TZVP/J Coulomb fitting basis for the resolution of identity[64,65] were used throughout. Unrelaxed potential energy surface scans were performed over DFT optimized geometries by applying several DFT functionals (BP86,[55,56] BLYP,[55,58] B3LYP[55,57,58] and B2PLYP[66]), as well as MP2 and the local-pair natural orbital coupled cluster (LPNO-CCSD)[67–69] methods. In addition, the effect of the dispersion correction for the DFT functionals was also tested.

DFT/ROCIS calculations were performed using the converged restricted Kohn–Sham RKS wavefunctions using the B3LYP/def2-TZVP calculation protocol together with the auxiliary basis set def2-TZVP/J in order to accelerate the calculations in the framework of RI approximation. Scalar relativistic effects were treated explicity by employing the implemented second-order Douglas–Kroll–Hess (DKH)[70–72] and ZORA[73] corrections. For the embedded cluster calculations capped effective core potentials

(*c*-ECPs) were used to replace the vanadium (ECP10MDF)[74] and oxygen (ECP2MWB)[75] atoms, respectively. In addition, calculations utilizing the conductor-like screening model (COSMO[76]) with an infinite dielectric constant were performed,[77–79] as implemented in ORCA.[80]

The cluster models for this study are described in detail below. The vanadium and oxygen atom positions were taken from the experimental X-ray bulk structure.[81]

Geometric properties

V_2O_5 crystalizes in an orthorhombic layer-type structure (*Pmmm*) based on zigzag double layers which extend perpendicular to the (010) direction, forming distorted VO_5 square pyramids sticking out at both sides of the layers. These layers possess three distinct and crystallographically inequivalent coordinated O centers. (a) The singly coordinated terminal/apical oxygen atoms O(1) which form relative short V–O bond lengths of about 1.578 Å and are aligned along the *c* molecular axis, (b) the two-fold coordinated bridging oxygen atoms, O(2) (V–O(2) = 1.779 Å), and (c) the three-fold coordinated oxygen atoms, O(3) (V–O(3) = 1.878 Å). In an alternative description, when looking along the (001) direction, the layers are weakly bound by Van der Waals electrostatic forces.[40,82,83] Along this view, the local vanadium environment assumes a highly distorted O_h geometry, thus forming a VO_6 core.[40,84] The distorted octahedron is formed because of the additional interlayered axial V–O(1′) bond (2.791 Å, Fig. 2).

Construction of cluster models

The cluster models that mimic the local environments of the V_2O_5 (010) and (001) crystal directions were constructed using the two most popular approaches, which involve hydrogen saturation or effective core potential embedding, respectively.

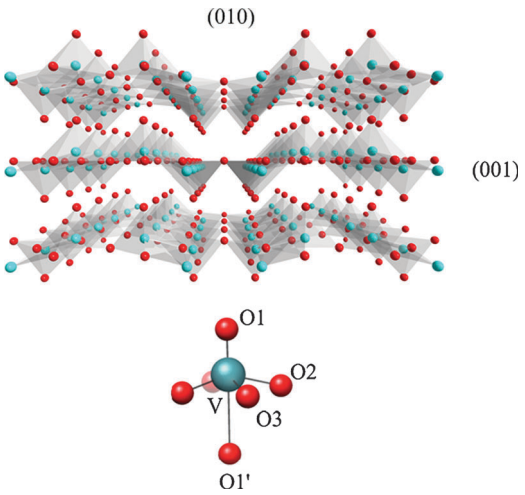

Fig. 2 Crystal structure of orthorhombic V_2O_5, which grows as an extended network along the (010) direction, forming a pentacoordinated vanadium center. These networks are packed in layers along the (001) direction in which vanadium obtains a local distorted octahedral environment. The different types of the O atoms (O(1), O(2), O(3) and O(1′)) coordinated to V are also illustrated.

Hydrogen saturation provides a simple and reasonable possibility to simulate bulk or surface properties, in which hydrogen atoms saturate the dangling bonds. This methodology has been widely applied in numerous V_2O_5 O K-edge core electron excitation studies.[34,85] The effect of the saturation is expected to primarily influence the O K-edge spectrum. Hence, the expectation is that larger clusters are required in order to correctly model these spectra. This will be discussed further in the following paragraphs. Initially, mono-layered clusters of increasing size were constructed along the (010) crystal direction (Fig. 2: $V_2O_9H_8$, $V_6O_{20}H_{10}$ and $V_{10}O_{31}H_{12}$). In a second step, double-layered clusters $V_4O_{18}H_{16}$, $V_{12}O_{40}H_{20}$ and $V_{20}O_{62}H_{24}$ were considered, in order to account for the weakly interacting crystal layers along the (001) direction (Fig. 3).

The embedded cluster approach provides a somewhat more rigorous approach for the calculation of the local properties of bulk surfaces.[86] Among several schemes proposed in the literature, in this study we use an approach where the whole cluster consists of three well defined regions presented in Scheme 1.[86] In this scenario, the quantum cluster (QC) is embedded in an extended point charge field (PC). Furthermore, in order to avoid electron attraction or electron-flow from the quantum cluster region towards the positive charges at the PC region, a third boundary region (BR) is introduced between those two, which consists of repulsive capped effective core potentials (*c*-ECPs). In order to allow for direct comparisons between the hydrogen saturated approach, the mono- and double-layered cluster models $[V_6O_{20}]^{-10}$ and $[V_{12}O_{40}]^{-20}$, respectively, were chosen to represent the QC regions. In this concept by choosing analogous BRs and PCs, one ensures charge neutrality of the embedded clusters. Traditionally PCs are chosen over the corresponding atom position on extended crystal super cells; however, the choice of the magnitude of these charges in either the BRs or PCs has been intensively debated in the literature.[86] Depending on the case under investigation, choices range from their formal values (as in the cases of strong ionic crystals MgO[87] and NiO[17,86]) to more sophisticated partial charges that are based on quantum mechanical calculations. The latter group of charges has mostly been used in more covalent cases such as in the studies of TiO_2.[88] Alternative choices have been reported as well.[16] Recent studies on rather covalent systems (*e.g.* hematite Fe_2O_3), used the formal charges of Fe (3+) and O (2−)[89,90] atoms.

A common feature of all these approaches is to conserve the charge neutrality conditions through special summation techniques to account for the shape and the size of the point charge field. However, the case of V_2O_5 is somewhat more complicated due to the highly anisotropic coordination environment around vanadium.[91] In fact as there are three different oxygen atoms (O(1), O(2) and O(3)), (Fig. 2), the point charge field will be composed by four different charges, namely qV, qO(1), qO(2) and qO(3). The experimental techniques for determining effective charges are rather ambiguous. The most accepted approach is to test whether the embedded system provides a reasonable description of the case under study by testing its ability to reproduce certain properties such as Madelung energies, as well as adsorption or excitation energies. In this work, the

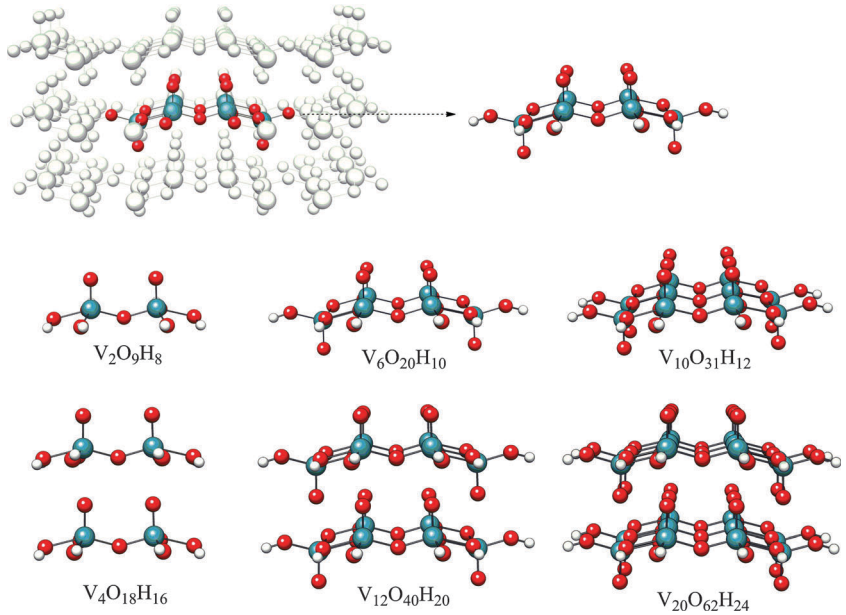

Fig. 3 Geometries of the hydrogen saturated cluster models representing the local pentacoordinated vanadium environment in the V_2O_5 (010) direction (mono-layered-models: $V_2O_9H_8$, $V_6O_{20}H_{10}$ and $V_{10}O_{31}H_{12}$). In addition, the local sections of the octahedrally coordinated vanadium centers along the (001) direction are also considered on the double-layered models: $V_4O_{18}H_{16}$, $V_{12}O_{40}H_{20}$ and $V_{20}O_{62}H_{24}$.

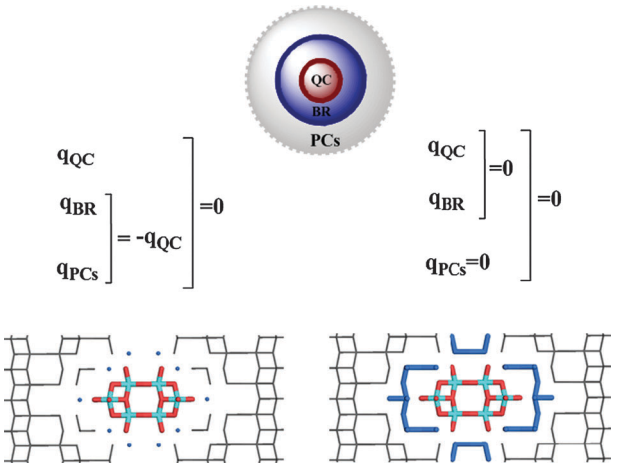

Scheme 1 Schematic representation of the general embedded method employed, as well as the two most significant embedding scenarios applied to achieve charge neutrality of the clusters.

efficiency of the chosen charges to reproduce core excitation spectra is thoroughly investigated. The coordinates of the charges to construct the point charge field are taken from the crystallographic coordinates of the corresponding atoms. These charges are then optimized towards predefined criteria of neutrality, as described below. Several layers with the most extended one reaching an upper limit of 55 029 charges control the size of the generated point charge fields. Furthermore, the QCs + BRs clusters were imposed either in the center of the generated point charge field or on its surface to account for bulk and surface effects, respectively. As can be seen in Scheme 1, two representative embedded cases have been investigated. In the first, reminiscent to the hydrogen saturation procedure, the V atoms that are bonded to the peripheral O atoms of the QC clusters are replaced by their respective *c*-ECPs and the full cluster is embedded in a point charge field by satisfying the charge neutrality condition: qQC = −(qBR + qPCs), where qs are the respective total charges. Alternatively, the boundary region can be chosen over V_xO_y fragments which together with the QC generate neutral periodic $(V_2O_5)_n$ slabs. In this second scenario, the charge neutrality condition is outlined by the relationship qQC + qBR = qPC = 0.

Weak interlayer interactions

As described above, the V_2O_5 is often referred to as a layered solid material, because the vanadyl oxygen atoms (O1′) point toward another vanadium atom of a neighboring layer, as described in the geometric properties section. The interlayer V–O(1′)···V distance is as short as 2.71 Å, resulting in interlayer interactions dominated by dispersion forces. DFT calculations incorporating van der Waals corrections have proven successful to describe the crystal lattice parameters, yielding a binding energy of ∼4–5 kcal mol^{-1} per V–O(1′)···V interacting pair, around the equilibrium X-ray distance.[92] Thus, in an effort to develop reliable double-layered cluster models along both the (010) and the (001) directions, we have constructed the V–O(1′)···V bond energy potential scans for the $V_4O_{18}H_{16}$ cluster model. Dispersion corrected DFT (DFT-D) methodologies including both pure hybrid and double hybrid functionals are considered together. In addition, more accurate *ab initio* MP2 and local pair natural orbitals CCSD (LPNO-CCSD) methods were employed. As shown in Fig. 4, both LPNO-CCSD, MP2, double hybrid DFT and DFT-D (GGA or hybrid-GGA) provide an accurate description of the interlayer weak V–O···V′ interactions. On the other hand, density functionals without vdW corrections perform, as expected, very poorly.

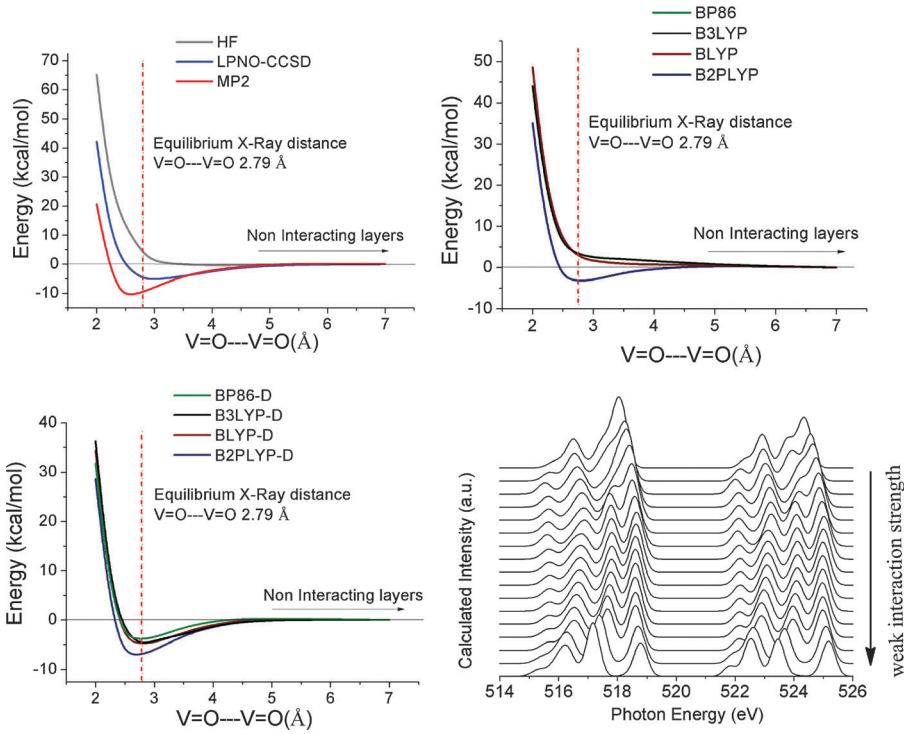

Fig. 4 PES scan along the weak interaction pathway V═O···V═O employing DFT, DFT-D, MP2 and LPNO-CCSD methods. The red dashed line indicates the X-ray equilibrium distance (2.79 A). In addition, $L_{2,3}$ DFT/ROCIS spectra are also calculated along the same pathway (bottom right).

These results demonstrate the suitability of the $V_4O_{18}H_{16}$ cluster model to describe the X-ray bulk structure of V_2O_5. Together with the extended $V_{12}O_{40}H_{20}$ and $V_{20}O_{62}H_{24}$ cluster models it is further used to calculate the V L-edge and K-edge spectra under the influence of the weakly interacting second layer.

Electronic structure

For the L-edge of $V^{(V)}$, the initial ground state is a singlet with electron configuration $2p^63d^0$. Upon one core 2p electron excitation to the valence shell, multiplets with a $2p^53d^1$ electron configuration occur. According to group theory considerations, the atomic multiplets that arise from this configuration are $^2P \otimes {}^2D = {}^{1,3}F, {}^{1,3}D, {}^{1,3}P$. These multiplets are subject to the following effects: (a) They are further split due to the ligand field, (b) they are mixed and split by SOC and (c) individual transitions are modulated in their intensities due to anisotropic covalency. All these effects together act to produce the actually observed L-edge pattern. In Fig. 5, the expected V-$2p_{xy}$ → V-3d and V-$2p_z$ → V-3d L-edge transitions (prior to SOC) are drawn in a one-electron picture, assuming local C_{4v} symmetry for the $V_2O_9H_8$ model hydrogen saturated dimer. Taking into account the degeneracy of all states involved under C_{4v} symmetry prior to SOC, it is illustrated in Fig. 5 that the $2p^53d^1$ configuration consists of 15 states which would result in a V L-edge spectrum with L_3/L_2 ratios (2 : 4 : 2 : 2)/(1 : 2 : 1 : 1), respectively. If this oversimplified description held, the L_3/L_2 ratio of NEXAFS spectrum of all the transition elements would be 2/1. Nevertheless, the one-electron picture is still useful for a qualitative description of the experimental and calculated spectra. At this level and under approximate C_{4v} symmetry, a total of 8 features are expected. In fact, as is illustrated in Fig. 5, the *xy* polarized XAS spectrum prior to SOC is dominated by 4 transitions of increasing energy, namely the $^1A_1 \rightarrow {}^{1,3}E$ ($2p_{xy} \rightarrow 3d_{xy}$) transition, followed by the $^1A_1 \rightarrow {}^{1,3}(A_1 + A_2 + B_1 + B_2)$ ($2p_{xy} \rightarrow 3d_{xz/yz}$), the $^1A_1 \rightarrow {}^{1,3}E$ ($2p_{xy} \rightarrow 3d_{x2-y2}$) and the $^1A_1 \rightarrow {}^{1,3}E$ ($2p_{xy} \rightarrow 3d_{z2}$) transitions. Similarly, the *z* polarized XAS spectrum is dominated by the $^1A_1 \rightarrow {}^{1,3}B_2$, $^1A_1 \rightarrow {}^{1,3}E$, $^1A_1 \rightarrow {}^{1,3}B_1$, and $^1A_1 \rightarrow {}^{1,3}A_1$ transitions.

The necessity, however, for a more quantitative description remains, requiring more elaborated approaches than the one-particle approximation, which properly treats the interaction between the multiplets involved in the formation of the L-edge spectrum. This has been successfully applied in the *ab initio* CTM approach;[14–17] however, to the best of our knowledge, it has never been done in a framework of the LS coupling scheme. In fact, action of SOC will further split and mix the ligand-field states into total of 60 magnetic spin sublevels, which are characterized by $m_S = 0, \pm 1$, and thus, it is usual to denote them as $|0\rangle$, $|+1\rangle$, $|-1\rangle$, respectively. Furthermore, due to dipole selection rules, among these 60 states in the C_{4v} symmetry, only 24 per vanadium atom will contribute to the spectrum.

Hydrogen saturated clusters

Calculations on the $V_2O_9H_8$ and $V_6O_{20}H_{10}$ V_2O_5 (010) surface cut-outs

The calculated V L-edge and O K-edge DFT/ROCIS absorption spectra for the monolayer $V_2O_9H_8$, $V_6O_{20}H_{10}$ and $V_{10}O_{31}H_{12}$ cut-outs of the V_2O_5 (010) direction (Fig. 2 and 3) are presented in Fig. 6.

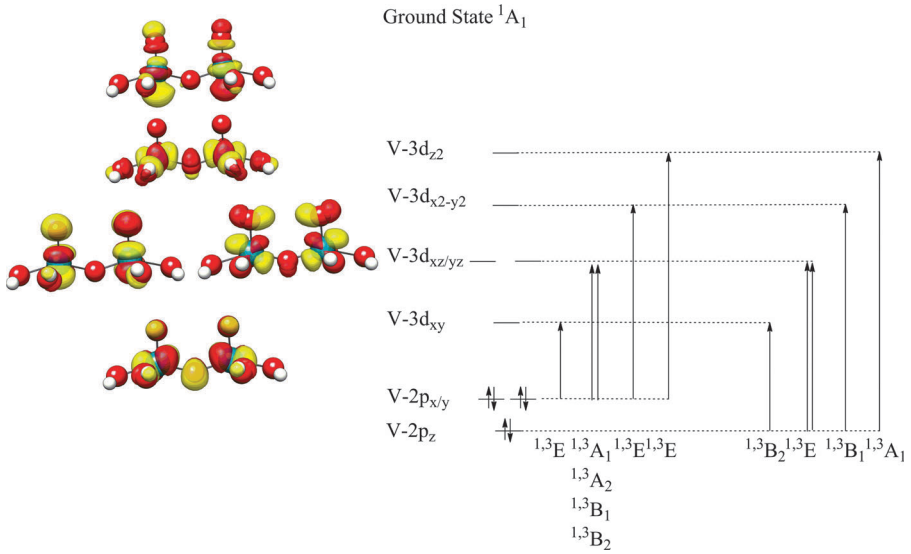

Fig. 5 MO orbital pictures of the $V_2O_9H_8$ dimer under C_{4v} symmetry, in a one electron particle/hole approximation. The V L-edge spectrum is constructed in terms of symmetry-adapted 2p → 3d transitions.

In all the cases, the calculated V L-edge and O K-edge spectra match the experimental spectrum very well. The L_3 region is well resolved, providing the most direct and detailed comparison between theory and experiment. It is noteworthy that the errors for the calculated L_2 and L_3 positions are slightly different. The 0.6 eV deviation (corresponding to 3–4% underestimation of the SOC splitting) has already been observed and discussed during the development of the DFT/ROCIS method

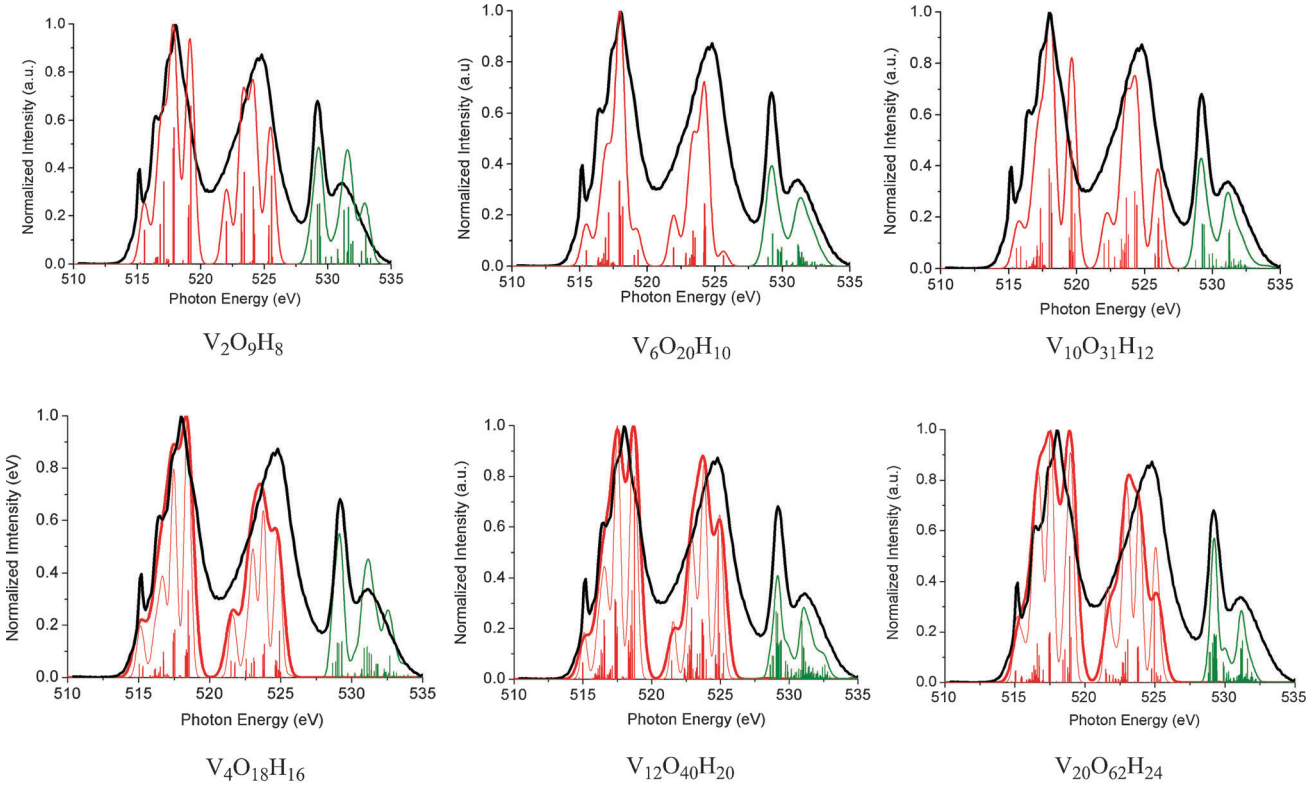

Fig. 6 DFT/ROCIS (B3LYP/def2-TZVP) V L-edge (red solid line) and O K-edge (green solid line) calculated spectra on the mono-layered hydrogen saturated cluster models (top): $V_2O_9H_8$, $V_6O_{20}H_{10}$ and $V_{10}O_{31}H_{12}$, as well as the corresponding double-layered models: $V_4O_{18}H_{16}$, $V_{12}O_{40}H_{20}$ and $V_{20}O_{62}H_{24}$ (bottom). The black thick line represents the background subtracted experimental powder spectrum. Red and green stick lines correspond to SOC corrected states. All calculated spectra have been energy shifted. A constant line shape broadening of 0.5 eV was applied for the monolayer models. In addition, for the interlayer clusters, a line shape broadening of 0.5 eV (thin red line) and correspondingly 1 eV (thick red line) were applied.

Table 1 Experimental data and B3LYP DFT/ROCIS based calculations for V L-edge and O K-edge absorption spectra. The element specific shifts (for V and O atoms) of the calculated spectra in order to match their experimental counterparts are reported for the various models used in the study

Experiment	% $L_{2,3}$/K ratio	V $L_{2,3}$-edge shift	O K-edge shift
$V_2O_5^{exp}$	61/39	—	—
Cluster models			
$V_2O_9H_8$	67/33	14.71	14.18
$V_6O_{20}H_{10}$	67/33	15.50	14.90
$V_{10}O_{31}H_{12}$	68/32	16.35	15.13
$V_4O_{18}H_{16}$	65/35	14.74	14.36
$V_{12}O_{40}H_{20}$	67/33	15.25	14.93
$V_{20}O_{62}H_{24}$	66/34	15.98	15.29
$[(V_6O_{20})^{-10}(BR + PC_1)]^0$	80/20	15.50	14.91
$[(V_{12}O_{40})^{-20}(BR + PC_2)]^0$	78/22	15.26	14.93
$[(V_6O_{20})^{-10}(BR)]^0$	77/23	15.49	14.90
$[(V_6O_{20})^{-10}(BR)]^0$ + COSMO	79/21	15.51	14.91
$[(V_6O_{20})^{-10}(BR)]^0$ + PC_3	75/25	15.52	14.91
$[(V_{12}O_{40})^{-20}(BR)]^0$	74/26	15.24	14.92
$[(V_{12}O_{40})^{-20}(BR)]^0$ + PC_4	73/27	15.25	14.93

PC_1 = 28 963, PC_2 = 28 959, PC_3 = 28 929, PC_4 = 28 927.

for transition metal L-edges.[23] Furthermore, a measure of the V–O covalency is provided by the ratio of the V $L_{2,3}$/O K-edge spectral areas. As can be seen in Table 1, in all the calculations, the V–O bonds are described to be slightly too ionic, indicating a less covalent V–O bond with respect to the experimental observations (Table 1). Another possible issue that complicated the comparison of theory and experiment is the partial reduction of V centers on the outermost layer of V_2O_5 due to the vacuum in combination with the X-ray beam.[44] Such possibility cannot be excluded and, hence, the true ratio of the relative intensities between V $L_{2,3}$-edge and O K-edge spectra of V_2O_5 cannot be unambiguously determined. We should note, however, that such effects are more pronounced in the surface sensitive XPS method and is less of an issue in NEXAFS measurements that operate in total electron yield mode. Obviously, accounting for such phenomena is clearly beyond the scope of the present study. Given these uncertainties, the reported calculated relative intensities given in Table 1 are considered to be in very good agreement with experiment.

For $V_{10}O_{31}H_{12}$, and all the other monolayer cluster models the DFT/ROCIS predicts wrong relative intensities for certain spectral features (Fig. 6). This observation reflects the anisotropic environment of the vanadium center, indicating that large cluster sizes are required in order to correctly reproduce the core excitation spectrum of V_2O_5. In addition, it should be highlighted that both the V L-edge and the O K-edge spectra carry complementary information on the covalent nature of the V–O bonds, as reflected in Fig. 7. The calculated states in the V L-region appear to have only a small degree of multiconfigurational character and, thus, offer a comprehensive picture of the electronic structure of the $L_{2,3}$ spectrum. The entire spectrum involves mainly spin conserving transitions, whereas the contribution of higher spin multiples is also significant, rising up to ~30–40%. In particular, the separated low energy future of the L_3 spectrum at 515 eV is dominated by the states $88\%|0\rangle + 12\%|\pm1\rangle$ involving the $2p \rightarrow 3d_{xy}$ single electron excitations, whereas the shoulder at 516 eV corresponds mainly to states $55\%|0\rangle + 45\%|\pm1\rangle$ originating from the $2p \rightarrow d_{xz/yz}$ single electron excitations. The most intense peak of the L_3 spectrum (517 eV) is dominated by the states $52\%|0\rangle + 48\%|\pm1\rangle$, which correspond to $2p \pm 3d_{x2-y2}$ excitations. Finally the shoulder at 519 eV is dominated by states of $88\%|0\rangle + 12\%|\pm1\rangle$ character, owing to $2p \rightarrow 3d_{z2}$ single electron excitations.

Weak interlayer interactions

Furthermore, we extend our discussion to the interlayer clusters $V_4O_{18}H_{16}$, $V_{12}O_{40}H_{20}$ and $V_{20}O_{62}H_{24}$. As shown in Fig. 7, the calculated spectra also appear to be in very good

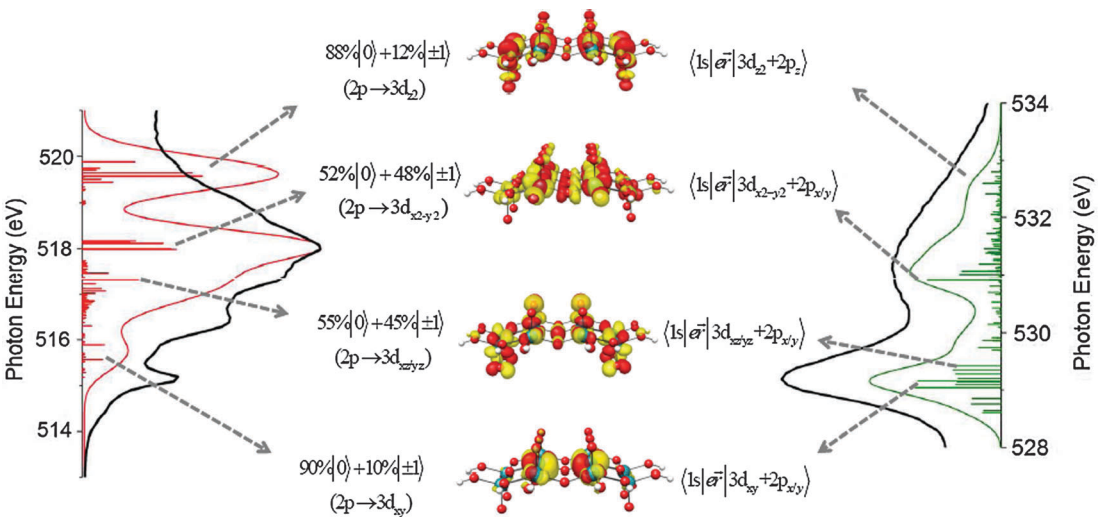

Fig. 7 Calculated B3LYP/ROCIS state contributions to the V L-edge (red) and O K-edge (green) spectra of the $V_{10}O_{31}H_{12}$ cluster model (green and red sticks, respectively). The dominant states are assigned in terms of magnetic sublevels, as well as one electron excitation V-2p → V-3d and O-1s → O-2p contributions. The local pentacoordinated environment of vanadium centers is illustrated in the corresponding MO pictures.

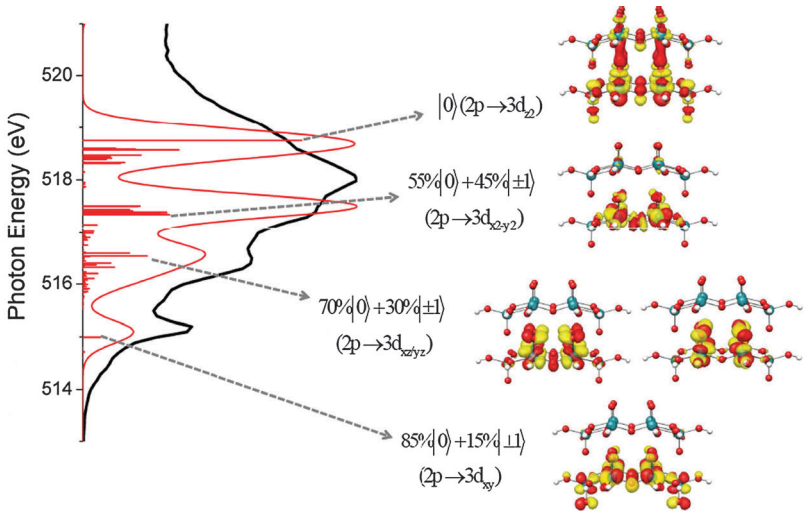

Fig. 8 Calculated B3LYP/ROCIS state contributions to the V L-edge (red, line broadening 0.5 eV) spectrum of the $V_{12}O_{40}H_{20}$ cluster model (red sticks). Similar to Fig. 7, the dominant states are assigned in terms of magnetic sublevels, as well as single electron excitation V-2p → V-3d and O-1s → O-2p contributions. Evidently, both the mono- and double-layered cluster models reflect a similar excitation pattern.

agreement with respect to experiment. Moreover, the cluster size effects are now smaller in comparison with the corresponding monolayer clusters. In fact, along the interlayer cluster series, the corresponding calculated V L-edge and O K-edge spectra look very similar. Size dependence effects are mainly observable only in the O K-edge spectrum of the smallest $V_4O_{18}H_{16}$ model. Furthermore, these spectra carry the same electronic information as their corresponding monolayer models. However, they are sharper in the V-L_3 region, when the same Gaussian broadening (0.5 eV) is applied. Looking at the $V_{12}O_{40}H_{20}$ cluster, as in the case of $V_{10}O_{31}H_{12}$, the L_3 spectrum is dominated by the states $85\%|0\rangle + 15\%|\pm1\rangle$ $70\%|0\rangle + 30\%|\pm1\rangle$ $55\%|0\rangle + 45\%|\pm1\rangle$ and almost pure $|0\rangle$ (>95%) involving the 2p → 3d_{xy} 2p → 3$d_{xz/yz}$ 2p → 3d_{x2-y2} and 2p → 3d_{z2} single electron excitations, respectively (Fig. 8). It is noteworthy that this latter set of excitations involves the interlayer interactions V–O(1′)···V and therefore serves the determining difference between the mono- and double-layered calculated spectra (Fig. 8). Evidently, by comparing the spectra of both the mono- and the interlayer clusters, the signals corresponding to *z*-polarized transitions 2p → 3$d_{xz/yz}$ and 2p → 3d_{z2} are underestimated in the case of the monolayer clusters. The signal intensity improves by considering more vanadyl bonds (V–O(1)) along the monolayer (010) plane, as in the case of $V_{10}O_{31}H_{12}$. Alternatively, this is achieved by considering the V′–(O1′)···V interaction in the interlayer clusters.

Up to this point of analysis, one can conclude that both the monolayer $V_{10}O_{31}H_{12}$ as well as the interlayer clusters $V_{12}O_{40}H_{20}$ and $V_{20}O_{62}H_{24}$ provide the required cluster size in order to satisfactorily calculate the core excitation spectra of V_2O_5.

Polarized spectra

In an effort to understand these effects in more detail, we now discuss the spatial distribution of the dipole transition moment for the monolayer clusters $V_6O_{20}H_{10}$ and $V_{10}O_{31}H_{12}$ (Fig. 9). These results are in excellent agreement with recent angular dependent[40] as well as DFT based angle dependent O K-edge NEXAFS studies.[34,36] Experimental single crystal spectra for V L-edge (up) and O K-edge (bottom) are presented in Fig. 9 with the beam polarization vector aligned perpendicular (normal incidence) or in a relation of about 30° (grazing incidence) with respect to the crystallographic *c* molecular axis. In the latter case, a significant component of the beam vector is parallel to the *c* molecular axis of the V_2O_5 single crystal; thus, these spectra show significant angle dependency. Likewise, the calculated spectra shown in Fig. 9 are strongly dependent on the transition dipole vector distribution. It is noticeable that for the smaller $V_6O_{20}H_{10}$, the *z*-polarized feature, corresponding to the 2p →3d_{z2} transitions, is highly underestimated, whereas, as discussed above, this same feature is significantly overestimated in the case of $V_2O_9H_8$ (Fig. 6). Therefore, a vital number of vanadyl bonds (V–O(1)) is required to describe the V_2O_5 surface in terms of core electron excited spectroscopy. Along the same lines, the O K-edge spectrum is highly polarized. In fact, the O K-edge peaks at 529 and 531 eV are dominated by the *z* and *xy* transition dipole allowed excitations O-1s → O-2p_{xy} and O-1s → O-2p_z, respectively, as shown in Fig. 5. Furthermore, the O K-edge spectrum is dominated by the vanadyl O(1) atom. It is therefore concluded that the V–O(1) interaction provides a spectral shape determinant which can be treated either by building a large monolayer cluster or by explicity treating the interlayer V′–(O1′)···V interactions in the interlayer cluster models. Therefore, a profound advantage of building interlayer clusters is that correct spectra are obtained with smaller clusters.

Bulk environment

The influence of the bulk environment is readily observed in the element dependent shifts for V and O atoms, respectively, as presented in Table 1. In fact, the shifts to match the highest experimental future at 518 eV (Fig. 1) are directly proportional

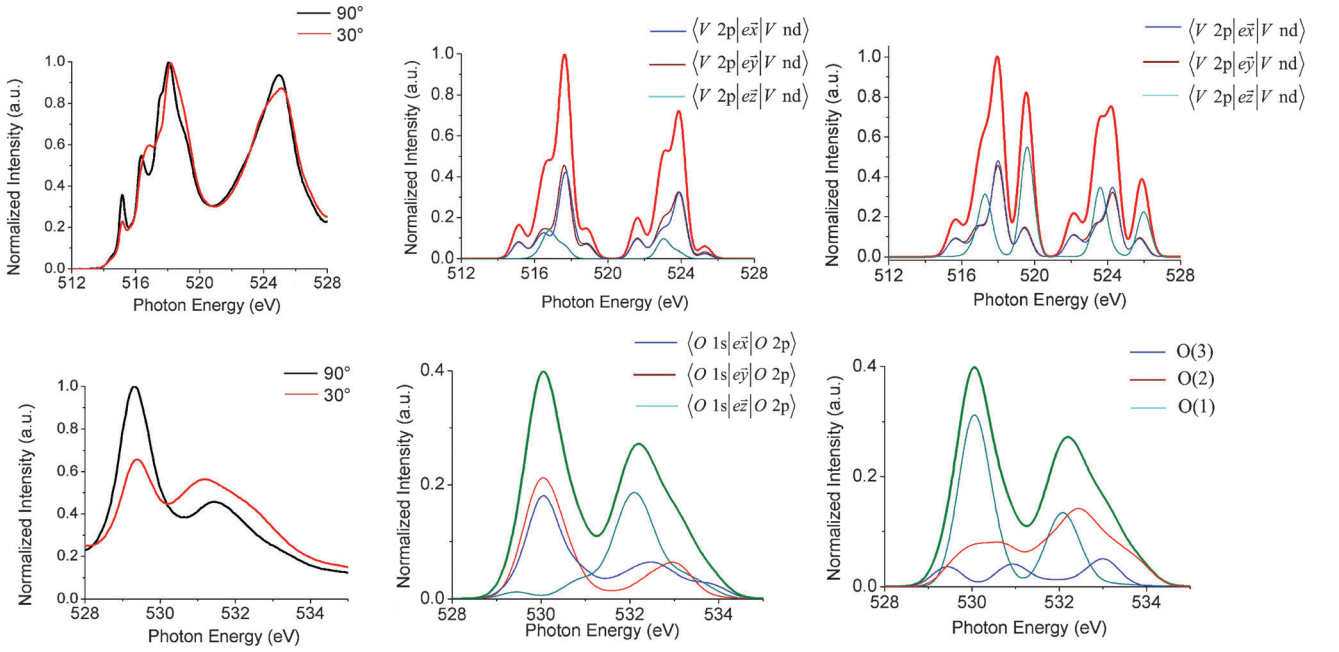

Fig. 9 Upper row: V L-edge single crystal spectra (left), B3LYP/def2-TZVP calculated V L-edge spectrum (red thick line) and transition dipole moments $\langle V\ 2p|\vec{er}|V\ nd\rangle$ for $V_6O_{20}H_{10}$ (middle) and $V_{10}O_{31}H_{12}$ (right). Bottom row: the corresponding calculated O K-edge single crystal spectra (left), and calculated spectra for $V_6O_{20}H_{10}$ together with dipole transition moments $\langle O\ 1s|\vec{er}|O\ 2p\rangle$ (middle) and the individual O atoms contributions (right).

to the number of the V atoms. Furthermore, two different shifting relations are observed for the monolayer and the interlayer cluster models for both V and O shifts (Table 1). This is due to the additional interaction of the second layer in the interlayered clusters. The net result is that the calculated spectra of the interlayer models shift to lower energies in comparison with the corresponding shift on the monolayer models. Furthermore, this is in agreement with the calculated $L_{2,3}$ spectra for the $V_4O_{18}H_{16}$ cluster along the calculated LPNO-CCSD weak interaction pathway (Fig. 4, bottom right). Indeed, the spectra shift towards lower energies ($\sim$0.3 eV) as the interaction between the isolated $V_2O_8H_9$ monomers increases. An alternative, therefore, to represent the calculated spectra is to superimpose and, subsequently, sum the $V_{10}O_{31}H_{12}$ V L- and O K-edge spectrum, which best describes the (010) crystal direction with the $V_{20}O_{62}H_{24}$ one which best describes the corresponding (001) direction. The net result is illustrated in Fig. 10a in which several contributions of the $V_{20}O_{62}H_{24}$ spectrum to the $V_{10}O_{31}H_{12}$ one are plotted. The best qualitative agreement with the experiment is observed for a contribution of about 40%, which is analysed in more detail in Fig. 10b. Similar results are observed when the influence between the monolayer $V_{10}O_{31}H_{12}$ and the interlayer $V_{12}O_{40}H_{20}$ spectra is considered (Fig. 10c). It is thus demonstrated that the treatment of the weakly interacting layers is crucial for the correct description of the bulk XAS spectrum of V_2O_5.

Embedded clusters

Furthermore, we extended our study on the periodic electrostatic embedded cluster calculations. The calculations were performed on neutral mono- and double- layered model clusters $[V_6O_{20}]^{10-}$ and $[V_{12}O_{40}]^{20-}$, respectively, using the embedding scheme described in the computational strategy section. In a wider perspective, these cluster models can be thought of as analogues of the corresponding hydrogen saturated $V_6O_{20}H_{10}$ and $V_{12}O_{40}H_{20}$ clusters, allowing for direct comparisons between the two methodologies. In the hydrogen saturated clusters, charge neutrality is achieved by completing the dangling bonds with hydrogen atoms, while in the embedded clusters the total charge neutrality is ensured by the BR + PCs or BR zones around them.

Point charges effect

As explained above, it is anything but trivial to choose the best possible combination of charges to equip the constructed point charge field. In this section we present an illustrative example for the $[(V_6O_{20})^{10-}(BR + PC_n)]^0$ embedded model, (PC_n = 28 929) (Scheme 1). In this system, there are more than 5×10^3 combinations among the 10^6 tested which can ensure the charge neutrality condition: qQC = qBR + qPCs $< 10^{-15}$. Among them, 12 characteristic combinations were chosen to span the wide range between 93% of the average formal ionic charges of vanadium and oxygen atoms (qV = +5 and qO(1) = qO(2) = qO(3) = −2) down to the lowest possible case reached in our test ($\sim$23%), as is shown in Table 2. For all these combinations, the V L-edge and O K-edge spectra have been calculated with the DFT/ROCIS method and the calculated spectra are plotted in Fig. 11. It can be clearly seen that the calculated spectra are very sensitive to the embedded charges used, a fact which is in sharp contrast with the respective observations for MgO[93] and TiO_2[94,95] embedded cluster models. In the case of $[(V_6O_{20})^{10-}(BR + PC_n)]^0$,

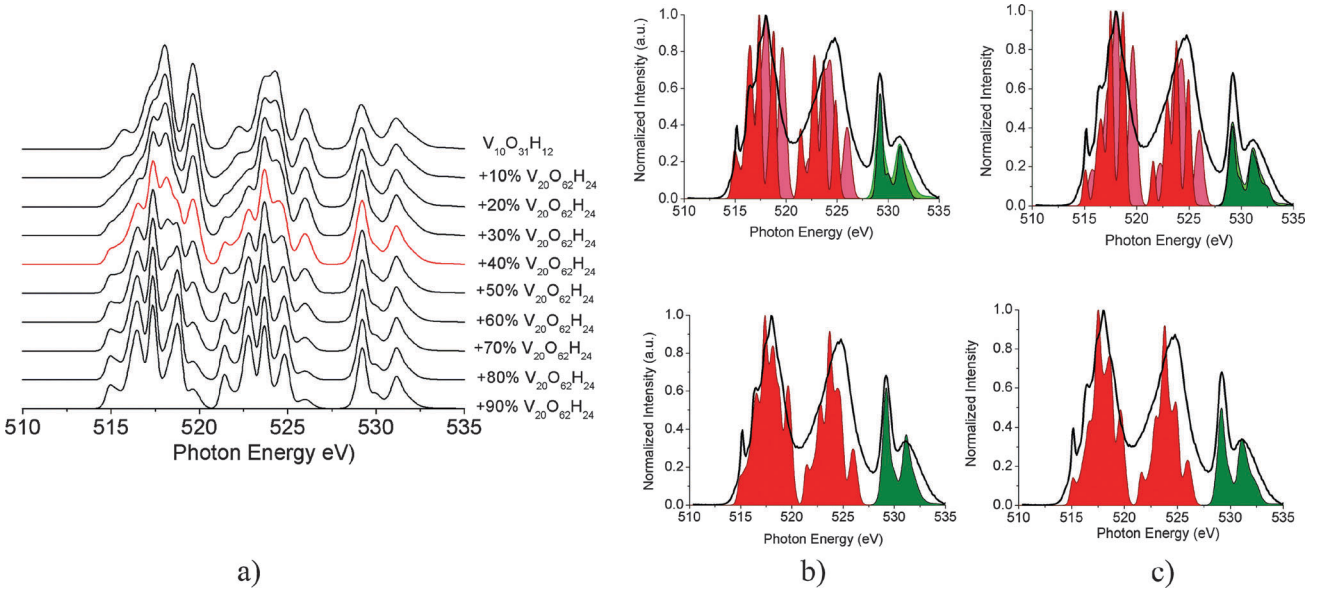

Fig. 10 (a) Calculation of $V_{10}O_{31}H_{12}$ V L-edge and O K-edge spectra with several contributions from the corresponding $V_{20}O_{62}H_{24}$ spectra. (b) Superposition (up) and summation (bottom) of the V L-edge and O K-edge spectra of $V_{10}O_{31}H_{12}$ and 40% $V_{20}O_{42}H_{24}$ spectra. (c) Superposition (up) and summation (bottom) of the V L-edge and O K-edge spectra of $V_{10}O_{31}H_{12}$ and $V_{12}O_{40}H_{20}$ spectra.

starting from average qPC values equal to 44% of the formal charges and above the calculated spectra decompose, as seen in Fig. 11. The best results for the V L-edge calculations within the studied set were observed using average qPCs = 27.3% of the formal ionic charges (Table 2), which agree well with the corresponding Mulliken charges.

Apart from the magnitude of the point charges, we have further investigated whether their size and their spatial distribution play any significant role in the calculated spectra. For accomplishing such calculations, the QC + ECP regions have been imposed either in the center of the point charge field (55 029 pcs) or on its most top surface (2830 pcs). The latter are extended up to a total number of 28 929 point charges along the *z*-direction (Fig. 12). In both cases the point charge field grows in layers along the coordinates defined by the (7 × 7 × 10) super-cell. As shown in Fig. 13 (left), the V L-edge spectra remain qualitatively and quantitatively unaffected by the number of the point charges used or the position of the QC + ECP region with respect to the point charge arrays. On the other hand, the K O-edge region is significantly affected by the number and the direction of the point charges. The most pronounced effect is obtained when the QC + ECP region is poised in the center of 55 029 point charges. The calculated spectrum appears to have substantial degree of *z*-polarization[40] as a result of charge strain around the vanadyl oxygen atoms, which mainly dominate the spectrum, as discussed above. It becomes evident from Fig. 13 that the most accurate description in terms of both V L-edge and O K-edge spectra is obtained when the QC-ECP region is embedded on the top surface of 28 929 point charges arrays. Thus, the latter embedded approach was used for all the cases examined by this procedure.

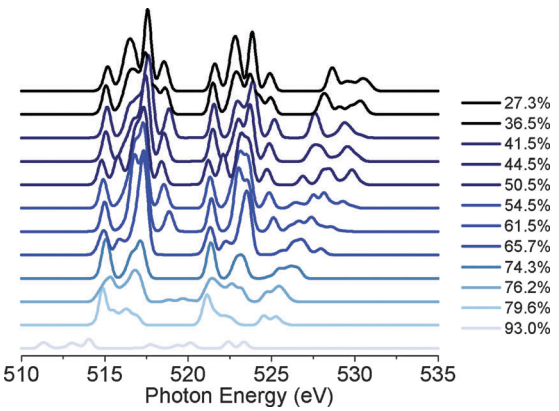

Fig. 11 Calculated V L-edge and O K-edge spectra for series of charges which span a wide range of covalent to ionic values regarding the formal charges of V:+5 and O:−2. The chosen combinations are presented in Table 2.

Table 2 Charges used to equip ECP and PC regions of the embedded scheme: $[(V_6O_{20})^{10-}(BR + QC_n)]^0$, ($PC_n$ = 28 929). They span a wide region between their most ionic values (~93% of their formal charges values) down to their most covalent ones (27.3%) of their formal covalent limit. All the chosen combinations could reduce the following charge neutrality condition: qQC − (qBR + qPCs) < 10^{-15}

%Av	V	O1	O2	O3
100.0	+5.00	−2.00	−2.00	−2.00
93.0	+4.56	−1.65	−2.00	−1.96
79.6	+3.92	−1.33	−1.83	−1.64
76.2	+3.76	−1.51	−1.56	−1.52
74.3	+3.64	−1.03	−1.79	−1.73
65.7	+3.28	−1.01	−1.69	−1.24
61.5	+3.00	−0.71	−1.63	−1.37
54.5	+2.80	−0.52	−1.88	−0.84
50.5	+2.52	−0.21	−1.81	−1.01
44.5	+2.20	−0.55	−1.22	−0.90
41.5	+2.04	−0.73	−0.92	−0.86
36.5	+1.76	−0.42	−0.92	−0.88
27.3	+1.40	−0.40	−0.80	−0.42

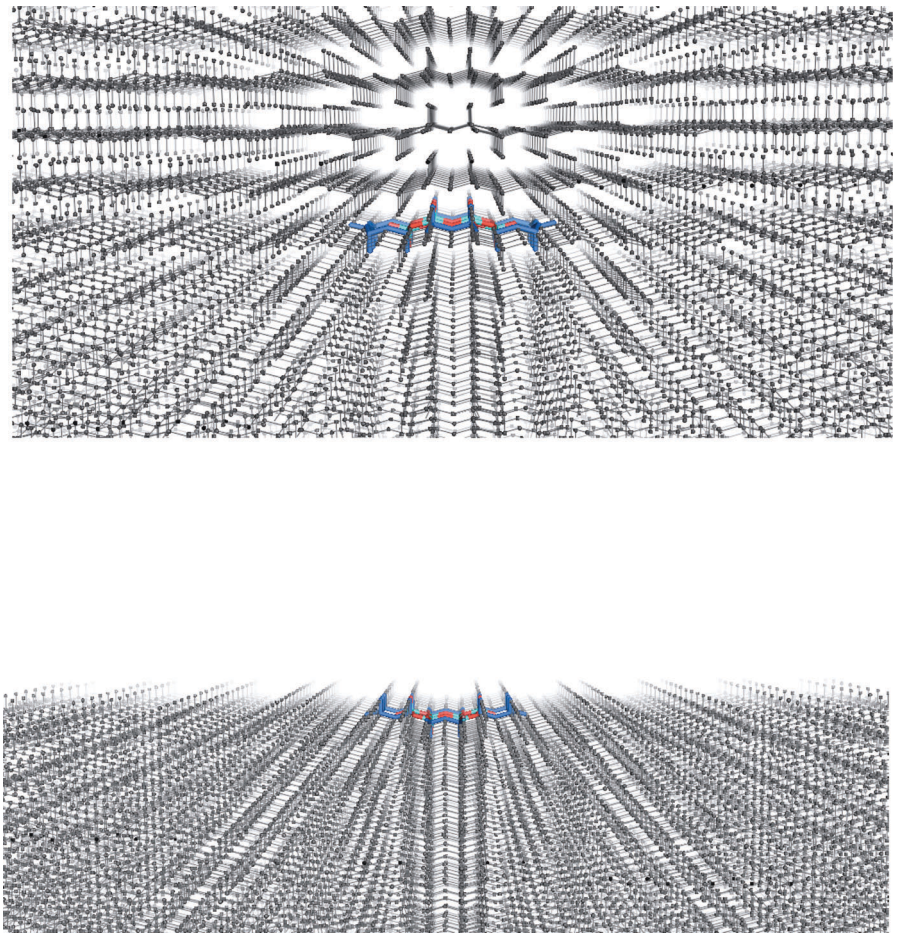

Fig. 12 Mono-layer clusters embedded in the middle or at the upper surface of the neutral point charge fields, PC_1 = 55 029, PC_2 = 28 929.

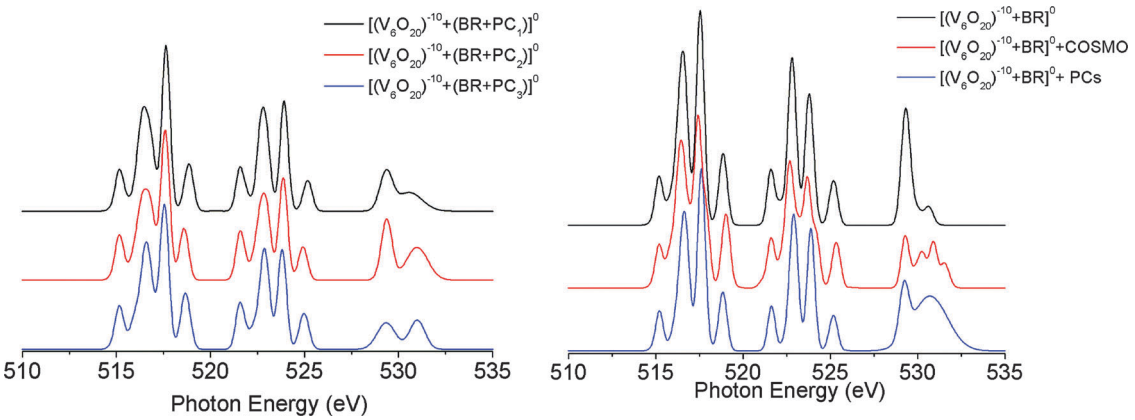

Fig. 13 Calculated V L-edge spectra; left: for the $[(V_6O_{20})^{10-}(BR + PC_n)]^0$ model embedded in different point charge arrays (PC_1 = 2830, PC_2 = 28 929, PC_3 = 55 029); right: for the neutral $[(V_6O_{20})^{10}(BR)]^0$ model, as well as upon embedding it in the COSMO potential with infinitive dielectric constant and the corresponding point charge field (PC = 28 964).

Calculation of V L-edge and O K-edge spectra with embedding schemes

As analyzed in the *calculation strategy* section, two embedding schemes were employed depending on whether the QC region is neutralized by the ECP + PC region or if the QC + ECP region gets pre-neutralized before it is embedded in a neutral PC field. This latter approach is interesting because it allowed us to test also other possibilities, such as the behavior of the neutralized QC + ECP region without the presence of an imposed electric field or the use of the COSMO contacting screening model in an

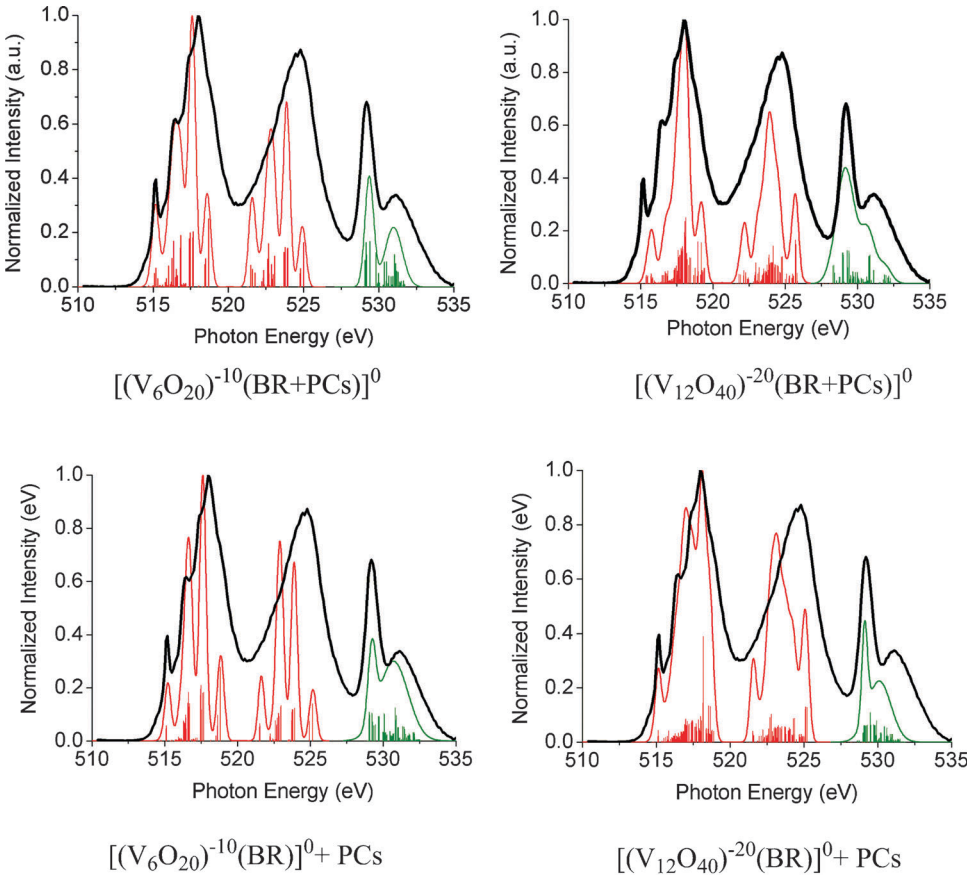

Fig. 14 DFT/ROCIS (B3LYP/def2-TZVP) V L-edge (red solid line) and O K-edge (green solid line) calculated spectra on the mono- and interlayer embedded cluster models following two embedding scenarios, (top): $[(V_6O_{20})^{10-}(BR + PCs)]^0$ and $[(V_{12}O_{40})^{20-}(BR + PCs)]^0$, (bottom): $[(V_6O_{20})^{10-}(BR)]^0$ + PCs and $[(V_{12}O_{40})^{20-}(BR)]^0$ + PCs. The black thick line represents the baseline subtracted experimental powder spectrum. Red and green stick lines correspond to SOC corrected states. PCs amount to about 29 000 point charges and they are explicitly presented in Table 1.

infinitive dielectric constant. Furthermore, as in the case of the hydrogen saturated clusters, both mono and double-layered QC cluster models were studied. At first, the calculated V L-edge and K O-edge spectra for the mono- $[(V_6O_{20})^{10-}(BR + PC_s)]^0$ and double-layered $[(V_{12}O_{40})^{20-}(BR + PC_s)]^0$ embedded clusters, respectively, are discussed. As shown in Fig. 14, the calculated V L-edge spectrum of the mono-layered cluster is already sharp and nicely resolved, reaching the quality of the interlayered hydrogen saturated clusters (Fig. 6). However, this model appears to be somewhat more ionic with respect to the hydrogen saturated cluster models, as can be seen from the V L-edge/O K-edge ratio (Table 1), as well as the Löwdin bond orders (Table 3).

Table 3 Average Löwdin bond orders for the calculated hydrogen saturated, as well as the embedded cluster models

Löwdin bond orders	V–O(1)	V–O(2)	V–O(3)
$V_{10}O_{31}H_{12}$	2.68	1.07	0.91
$V_{20}O_{62}H_{24}$	2.70	1.03	0.91
$[(V_6O_{20})^{-10}(BR + PC_1)]^0$	2.48	1.17	0.89
$[(V_{12}O_{40})^{-10}(BR + PC_2)]^0$	2.37	1.14	0.90
$[(V_6O_{20})^{-20}(BR)]^0 + PC_3$	2.32	1.31	0.71
$[(V_{12}O_{40})^{-20}(BR)]^0 + PC_4$	2.31	1.28	0.73

PC_1 = 28 963 PC_2 = 28 959, PC_3 = 28 929, PC_4 = 28 927.

This situation is partially reduced when the interlayered model is applied. In fact, as more transitions are involved, the spectrum gets broader; however, the bulk environment is still not correctly reproduced, indicating the necessity to use more covalent model systems. In the second embedding approach performed on mono- and double-layered BR-neutralized clusters, $[(V_6O_{20})^{10-}(BR)]^0$ and $[(V_6O_{20})^{20-}(BR)]^0$, the effect of the embedded medium was initially investigated. As shown in Fig. 13 (right), the V L-edge region remains almost unaffected independent of whether the QC + BR region is employed alone or embedded in PCs or the COSMO electric potentials. The quality of the K O-edge spectrum on the other hand is clearly reduced when COSMO is applied; in line with the first embedding case, PC arrays ~29 000 (Table 1) are chosen for the persistent analysis. The corresponding calculated spectra for the mono- $[(V_6O_{20})^{10-}(BR)]^0$ + PC_S and double-layered $[(V_{12}O_{40})^{20-}(BR)]^0$ + PC_S clusters are shown in Fig. 14. In comparison to the first embedding scheme, the ratio of the $L_{2,3}$/K region is somewhat smaller, indicating a more covalent model (Tables 1 and 3). In the most pronounced case of the double-layered model, the $L_{2,3}$ spectra are nicely broadened, while more than four features are now observed per L region, indicating significant contribution from the bulk environment. In addition, the O K-edge spectrum

has the correct shape. Hence, in spite of some remaining shortcomings owing to the underestimation of V–O covalency and the fact that the model is still too small to fully describe the spectral influences originating from the bulk environment, the obtained results with this embedded model are satisfactory.

Conclusion on the choice of cluster modeling

In summary, we have compared the hydrogen saturation and embedding techniques. As far as the V L-edge spectrum is concerned, both techniques perform satisfactorily when double-layered clusters are chosen. Anisotropic broadening is observed directly in the case of the embedded interlayered clusters, accounting for the effect of the bulk. Thus, the embedding technique together with sufficiently large clusters appears to be the method of choice. With respect to the O K-edge spectrum and the $L_{2,3}$/K relative intensities, the hydrogen-saturated procedure provided better agreement with experiment. In this case, the latter technique applied to interlayer clusters of the proper size is the method of choice.

Conclusions

A systematic theoretical study of the V L-edge and O K-edge spectra of V_2O_5 spectra is presented by applying the newly developed DFT/ROCIS method. In order to enter the field of solid-state core electron spectroscopy, we followed traditional methodologies such as the hydrogen saturation, as well as the embedded cluster model procedures. The generally good to excellent agreement between experiment and theory allowed for a more detailed *in silico* investigation of the contributions to the experimental core electron absorption spectra. The spectra are dominated by transitions that show only little multi-configurational character. Therefore, a molecular LS coupling picture is required to account for the quantitative nature of the observed experimental features. Under the hydrogen saturation process, model systems up to $V_{20}O_{62}H_{24}$ were utilized, accounting for both surface and bulk effects. In fact, it was shown that the influence of the second layer on the spectrum is very significant, originating from weakly interacting crystal layers. In a quantitative and qualitative manner, better results with this approach are obtained when surface and bulk effects were firstly treated separately on mono- and double-layered clusters, respectively, and incorporated together in a second step. In addition, several embedded cluster models scenarios were investigated. For this purpose, the cluster models were built accordingly to the hydrogen saturated models. The aim was to first optimize several parameters prior to the calculation of the core electron excitation spectra. In fact it was shown that the charges to construct the point charge field and, thus, its strength, are very important, whereas the size of the charge field above a minimum value is not crucial. The embedded clusters were found to be rather ionic, compared with the more covalent hydrogen saturated ones. This is a fact, which largely influences the shape and the intensity of the calculated O K-edge spectrum. However, the distribution of the surface and bulk properties could be reproduced with much smaller models than those needed with the hydrogen saturated procedure. In a more general perspective, the DFT/ROCIS study presented herein forms the basis for future quantitative studies of NEXAFS spectra in the wider area of *in situ* solid state catalysis.[35,44,96–101]

Abbreviations

NEXAFS	Near edge X-ray absorption fine structure
DFT	density functional theory
ROCIS	restricted open shell configuration interaction with singles
SOC	spin–orbit coupling
LF	ligand field
QDPT	quasi degenerate perturbation theory.

Acknowledgements

FN and RS gratefully acknowledge financial support of this work by the Max Planck Society. The Helmholtz-Zentrum Berlin (HZB) staff is acknowledged for continuously supporting the synchrotron based near ambient pressure spectroscopy experiments of the Fritz Haber Institute at BESSY II.

References

1 F. M. F. de Groot and A. Kotani, *Core Level Spectroscopy of Solids*, CRC Press, 2008.
2 J. G. Chen, *Surf. Sci. Rep.*, 1997, **30**, 1–152.
3 A. I. Nesvizhskii and J. J. Rehr, *J. Synchrotron Radiat.*, 1999, **6**, 315–316.
4 S. DeBeer George and F. Neese, *Inorg. Chem.*, 2010, **49**, 1849–1853.
5 S. DeBeer George, T. Petrenko and F. Neese, *Inorg. Chim. Acta*, 2008, **361**, 965.
6 S. DeBeer George, T. Petrenko and F. Neese, *J. Phys. Chem. A*, 2009, **112**, 12936.
7 M. G. Brik, K. Ogasawara, H. Ikeno and I. Tanaka, *Eur. Phys. J. B*, 2006, **51**, 345–355.
8 R. De Francesco, M. Stener, M. Causa, D. Toffoli and G. Fronzoni, *Phys. Chem. Chem. Phys.*, 2006, **8**, 4300–4310.
9 G. Fronzoni, R. D. Francesco and M. Stener, *J. Chem. Phys.*, 2012, **137**, 224308.
10 F. M. F. de Groot, *Coord. Chem. Rev.*, 2005, **249**, 31–63.
11 F. M. F. de Groot, *J. Electron Spectrosc. Relat. Phenom.*, 1994, **67**, 529–622.
12 A. Kotani, *J. Electron Spectrosc. Relat. Phenom.*, 1999, **100**, 75–104.
13 E. C. Wasinger, F. M. F. de Groot, B. Hedman, K. O. Hodgson and E. I. Solomon, *J. Am. Chem. Soc.*, 2003, **125**, 12894–12906.
14 H. Ikeno, T. Mizoguchi and I. Tanaka, *Phys. Rev. B: Condens. Matter Mater. Phys.*, 2011, **83**, 155107.
15 H. Ikeno, I. Tanaka, Y. Koyama, T. Mizoguchi and K. Ogasawara, *Phys. Rev. B: Condens. Matter Mater. Phys.*, 2005, **72**, 075123.

16 Y. Kumagai, H. Ikeno, F. Oba, K. Matsunaga and I. Tanaka, *Phys. Rev. B: Condens. Matter Mater. Phys.*, 2008, **77**, 155124.
17 K. Ogasawara, T. Iwata, Y. Koyama, T. Ishii, I. Tanaka and H. Adachi, *Phys. Rev. B: Condens. Matter Mater. Phys.*, 2001, **64**, 115413.
18 P. Krueger and C. R. Natoli, *Phys. Rev. B: Condens. Matter Mater. Phys.*, 2004, **70**, 245120.
19 C. R. Natoli, M. Benfatto, C. Brouder, M. F. Lopez and D. L. Foulis, *Phys. Rev. B: Condens. Matter Mater. Phys.*, 1990, **42**, 1944–1968.
20 A. L. Ankudinov, A. I. Nesvizhskii and J. J. Rehr, *Phys. Rev. B: Condens. Matter Mater. Phys.*, 2003, **67**, 115120.
21 M. Haverkort, M. Zwierzycki and O. Andersen, *Arxiv preprint arXiv:1111.4940*, 2011.
22 P. S. Bagus, H. Freund, H. Kuhlenbeck and E. S. Ilton, *Chem. Phys. Lett.*, 2008, **455**, 331–334.
23 M. Roemelt, D. Maganas, S. DeBeer and F. Neese, *J. Chem. Phys*, submitted.
24 C. M. Marian and U. Wahlgren, *Chem. Phys. Lett.*, 1996, **251**, 357–364.
25 B. A. Hess, C. M. Marian, U. Wahlgren and O. Gropen, *Chem. Phys. Lett.*, 1996, **251**, 365–371.
26 F. Neese, *J. Chem. Phys.*, 2005, **122**, 34107.
27 P. Forzatti, *Appl. Catal., A*, 2001, **222**, 221.
28 E. A. Mamedov and V. Cortés Corberán, *Appl. Catal., A*, 1995, **127**, 1–40.
29 J. Haber, M. Witko and R. Tokarz, *Appl. Catal., A*, 1997, **157**, 3–22.
30 E. E. Chain, *Appl. Opt.*, 1991, **30**, 2782.
31 M. Winter, O. B. Jurgen, M. E. Spahr and P. Novak, *Adv. Mater.*, 1998, **10**, 725.
32 M. S. Whittingham, *J. Electrochem. Soc.*, 1976, **123**, 315.
33 D. W. Murphy, P. A. Christian, F. J. DiSalvo and J. V. Waszczak, *Inorg. Chem.*, 1979, **18**, 2800.
34 C. Kolczewski and K. Hermann, *Phys. Scr.*, 2005, **T115**, 128.
35 M. Cavalleri, K. Hermann, A. Knop-Gericke, M. Hävecker, R. Herbert, C. Hess, A. Oestereich, J. Döbler and R. Schlögl, *J. Catal.*, 2009, **262**, 215–223.
36 C. Kolczewski and K. Hermann, *Surf. Sci.*, 2004, **552**, 98–110.
37 D. M. Bishop, *Group Theory And Spectroscopy*, Dover, New York, 1973.
38 D. C. Harris and M. D. Bertolucci, *Symmetry And Spectroscopy. An Introduction to Vibrational and Electronic Spectroscopy*, Dover, New York, 1978.
39 In order to make the comparison with theory feasible continuum absorption together with the O K-edge absorption beyond 535 eV have been subtracted.
40 J. M. Velazquez, C. Jaye, D. A. Fischer and S. Banerjee, *J. Phys. Chem. C*, 2009, **113**, 7639–7645.
41 D. Coster and R. D. L. Kronig, *Physica*, 1935, **2**, 13–24.
42 L. Whittaker, H. Zhang and S. Banerjee, *J. Mater. Chem.*, 2009, **19**, 2968–2974.
43 C. Hébert, M. Willinger, D. S. Su, P. Pongratz, P. Schattschneider and R. Schlögl, *Eur. Phys. J. B*, 2002, **28**, 407–414.
44 M. Hävecker, M. Cavalleri, R. Herbert, R. Follath, A. Knop-Gericke, C. Hess, K. Hermann and R. Schlögl, *Phys. Status Solidi B*, 2009, **246**, 1459–1469.
45 F. Jachmann and C. Hucho, *Solid State Commun.*, 2005, **135**, 440–443.
46 R. McWeeny, *Methods of Molecular Quantum Mechanics*, Academic Press, London, 2012.
47 F. Neese, T. Petrenko, D. Ganyushin and G. Olbrich, *Coord. Chem. Rev.*, 2007, **251**, 288–327.
48 F. Neese, W. Ames, G. Christian, M. Kampa, D. G. Liakos, D. A. Pantazis, M. Roemelt, P. Surawatanawong and Y. E. Shengfa, in *Advances in Inorganic Chemistry*, ed. E. Rudi van and H. Jeremy, Academic Press, 2010, vol. 62, pp. 301–349.
49 T. Glaser, B. Hedman, K. O. Hodgson and E. I. Solomon, *Acc. Chem. Res.*, 2000, **33**, 859–868.
50 S. DeBeer George, T. Petrenko and F. Neese, *Inorg. Chim. Acta*, 2008, **361**, 965–972.
51 N. Lee, T. Petrenko, U. Bergmann, F. Neese and S. DeBeer, *J. Am. Chem. Soc.*, 2010, **132**, 9715–9727.
52 M. Roemelt, M. A. Beckwith, C. Duboc, M.-N. Collomb, F. Neese and S. DeBeer, *Inorg. Chem.*, 2011, **51**, 680–687.
53 D. Maganas, R. Roemelt, T. Weyhermüller, R. Blume, M. Hävecker, A. K. Gericke, S. DeBeer, R. Schlögl and F. Neese, in preparation.
54 F. Neese, *Wiley Interdiscip. Rev.: Comput. Mol. Sci.*, 2012, **2**, 73–78.
55 A. D. Becke, *Phys. Rev. A: At., Mol., Opt. Phys.*, 1988, **38**, 3098–3100.
56 J. P. Perdew, *Phys. Rev. B: Condens. Matter Mater. Phys.*, 1986, **33**, 8822–8824.
57 A. D. Becke, *J. Chem. Phys.*, 1993, **98**, 5648.
58 C. Lee, W. Yang and R. G. Parr, *Phys. Rev. B: Condens. Matter Mater. Phys.*, 1988, **37**, 785.
59 S. Grimme, J. Antony, S. Ehrlich and H. Krieg, *A consistent and accurate ab initio parametrization of density functional dispersion correction (DFT-D) for the 94 elements H–Pu*, AIP, 2010.
60 S. Grimme, S. Ehrlich and L. Goerigk, *J. Comput. Chem.*, 2011, **32**, 1456–1465.
61 A. Schafer, H. Horn and R. Ahlrichs, *J. Chem. Phys.*, 1992, **97**, 2571.
62 F. Weigend and R. Ahlrichs, *Phys. Chem. Chem. Phys.*, 2005, **7**, 3297.
63 A. Schäfer, C. Huber and R. Ahlrichs, *J. Chem. Phys.*, 1994, **100**, 5829–5835.
64 M. Feyereisen, G. Fitzgerald and A. Komornicki, *Chem. Phys. Lett.*, 1993, **208**, 359.
65 R. A. Kendall and H. A. FrÃáchtl, *Theor. Chem. Acc.*, 1997, **97**, 158.
66 S. Grimme, *J. Chem. Phys.*, 2006, **124**, 034108.
67 D. G. Liakos, A. Hansen and F. Neese, *J. Chem. Theory Comput.*, 2010, **7**, 76.
68 J. P. Perdew, *Phys. Rev. B: Condens. Matter Mater. Phys.*, 1986, **33**, 8522.
69 F. Neese, *Coord. Chem. Rev.*, 2009, **253**, 526–563.

70 B. A. Hess, *Phys. Rev. A: At., Mol., Opt. Phys.*, 1985, **32**, 756.
71 B. A. Hess, *Phys. Rev. A: At., Mol., Opt. Phys.*, 1986, **333**, 3742.
72 G. Jansen and B. A. Hess, *Phys. Rev. A: At., Mol., Opt. Phys.*, 1989, **39**, 6016.
73 D. A. Pantazis, X. Y. Chen, C. R. Landis and F. Neese, *J. Chem. Theory Comput.*, 2008, **4**, 908.
74 M. Dolg, U. Wedig, H. Stoll and H. Preuss, *J. Chem. Phys.*, 1987, **86**, 866.
75 A. Bergner, M. Dolg, W. Küchle, H. Stoll and H. Preuß, *Mol. Phys.*, 1993, **80**, 1431–1441.
76 A. Klamt and G. Schuurmann, *J. Chem. Soc., Perkin Trans. 2*, 1993, 799.
77 J. Tomasi, *Theor. Chem. Acc.*, 2004, **112**, 184.
78 J. Tomasi and M. Persico, *Chem. Rev.*, 1994, **94**, 2027.
79 C. J. Cramer and D. G. Truhlar, *Chem. Rev.*, 1999, **99**, 2161.
80 S. Sinnecker, A. Rajendran, A. Klamt, M. Diedenhofen and F. Neese, *J. Phys. Chem. A*, 2006, **110**, 2235.
81 R. Enjalbert and J. Galy, *Acta Crystallogr., Sect. C: Cryst. Struct. Commun.*, 1986, **C42**, 1467–1469.
82 T. s. Bučko, J. R. Hafner, S. B. Lebègue and J. N. G. Ángyán, *J. Phys. Chem. A*, 2010, **114**, 11814–11824.
83 E. Londero and E. Schröder, *Phys. Rev. B: Condens. Matter Mater. Phys.*, 2010, **82**, 054116.
84 M. Willinger, N. Pinna, D. S. Su and R. Schlöegl, *Phys. Rev. B: Condens. Matter Mater. Phys.*, 2004, **69**, 155114.
85 C. Kolczewski and K. Hermann, *J. Chem. Phys.*, 2003, **118**, 7599–7609.
86 V. Staemmler, The Cluster Approach for the Adsorption of Small Molecules on Oxide Surfaces, in *Theorectical Aspects of Transition Metal Catalysis*, ed. G. Frenking, Springer, Berlin/Heidelberg, 2005, vol. 12, pp. 219–256.
87 Y. Kawamura and H. Nakai, *Chem. Phys. Lett.*, 2005, **410**, 64–69.
88 S. C. Ammal and A. Heyden, *J. Chem. Phys.*, 2010, **133**, 164703–164715.
89 P. Liao and E. A. Carter, *J. Phys. Chem. C*, 2011, **115**, 20795–20805.
90 P. Liao, M. C. Toroker and E. A. Carter, *Nano Lett.*, 2011, **11**, 1775–1781.
91 A. Chakrabarti, K. Hermann, R. Druzinic, M. Witko, F. Wagner and M. Petersen, *Phys. Rev. B: Condens. Matter Mater. Phys.*, 1999, **59**, 10583–10590.
92 X. Yin, A. Fahmi, A. Endou, R. Miura, I. Gunji, R. Yamauchi, M. Kubo, A. Chatterjee and A. Miyamoto, *Appl. Surf. Sci.*, 1998, **130–132**, 539–544.
93 C. H. Hu and D. P. Chong, *Chem. Phys. Lett.*, 1995, **262**, 729.
94 M. Stener, A. Lisini and P. Decleva, *Chem. Phys. Lett.*, 1995, **191**, 141.
95 G. Fronzoni, R. De Francesco, M. Stener and M. Causà, *J. Phys. Chem. B*, 2006, **110**, 9899–9907.
96 M. Hävecker, A. Knop-Gericke, H. Bluhm, E. Kleimenov, R. W. Mayer, M. Fait and R. Schlögl, *Appl. Surf. Sci.*, 2004, **230**, 272–282.
97 M. Hävecker, N. Pinna, K. Weiß, H. Sack-Kongehl, R. E. Jentoft, D. Wang, M. Swoboda, U. Wild, M. Niederberger, J. Urban, D. S. Su and R. Schlögl, *J. Catal.*, 2005, **236**, 221–232.
98 E. Kleimenov, H. Bluhm, M. Hävecker, A. Knop-Gericke, A. Pestryakov, D. Teschner, J. A. Lopez-Sanchez, J. K. Bartley, G. J. Hutchings and R. Schlögl, *Surf. Sci.*, 2005, **575**, 181–188.
99 K. Alexopoulos, P. Hejduk, M. Witko, M.-F. Reyniers and G. B. Marin, *J. Phys. Chem. C*, 2010, **114**, 3115–3130.
100 B. Beck, M. Harth, N. G. Hamilton, C. Carrero, J. J. Uhlrich, A. Trunschke, S. Shaikhutdinov, H. Schubert, H.-J. Freund, R. Schlögl, J. Sauer and R. Schomäcker, *J. Catal.*, 2012, **296**, 120–131.
101 C. Popa, M. a. V. n. Ganduglia-Pirovano and J. Sauer, *J. Phys. Chem. C*, 2011, **115**, 7399–7410.

